Dynamics of jets produced by bursting bubbles

Luc Deike,[1,2,*] Elisabeth Ghabache,[3] Gérard Liger-Belair,[4] Arup K. Das,[5] Stéphane Zaleski,[3] Stéphane Popinet,[3] and Thomas Séon[3]

[1]*Department of Mechanical and Aerospace Engineering, Princeton University, Princeton, New Jersey 08544, USA*

[2]*Princeton Environmental Institute, Princeton University, Princeton, New Jersey 08544, USA*

[3]*Sorbonne Universités, Université Pierre et Marie Curie and Centre National de la Recherche Scientifique, Unité Mixte de Recherche 7190, Institut Jean Le Rond d'Alembert, 4 Place Jussieu, F-75005 Paris, France*

[4]*Equipe Effervescence (GSMA), UMR CNRS 7331, Université de Reims Champagne-Ardenne, BP 1039, 51687 Reims, France*

[5]*Department of Mechanical and Industrial Engineering, IIT Roorkee, Roorkee 247667, India*

(Received 1 August 2017; published 25 January 2018)

Sea spray is the main source of aerosols above the ocean. One of the pathways for sea spray production is through bubble bursting, which ejects myriads of droplets. We present a detailed description of the velocity of jets formed by bubble bursting, obtained through extensive comparison between experimental results and numerical simulations for a wide range of physical parameters. We discuss the importance of the shape of the cavity on the jet velocity and the regime of parameters for which drop ejection is observed. We present a phenomenological formula that predicts the jet velocity for the full range of parameters and compare it to a theoretical prediction based on curvature reversal. The results are then discussed in light of their fundamental applications in the understanding of the phenomena.

DOI: 10.1103/PhysRevFluids.3.013603

I. INTRODUCTION

Ocean spray is composed of small liquid droplets formed through two main pathways: the spume drops, produced from the tearing of breaking wave crests by strong winds [1,2] and the film and jet drops produced by bursting bubbles [3–7], after a breaking wave event has entrained air below the sea surface [8–10]. These drops play a crucial role in the exchange between the ocean and atmosphere by transporting water, heat, dissolved gases, salts, surfactants, and biological materials. Once transported in the upper atmosphere, they may evaporate, affect the radiative balance of the atmosphere, and serve as cloud condensation nuclei [11–14]. After a bubble reaches the free surface, the thin liquid film separating the bubble from the atmosphere drains and disintegrates producing film drops [15]. This process leaves an unstable opened cavity which collapse [7,16,17] and eventually throw jet drops [18] mainly vertically above the surface, through the formation and eventually the break up of a rising jet (see Figs. 1, 2, and 3). This latter mechanism is thought to account for sea spray aerosol particles in the atmosphere with radii between 1 and 200 μm [14]. A recent study shows that the chemical composition of small jet drops differs from those of film drops and discusses implications for atmospheric chemistry [19]. The generation of ocean spray by bursting bubbles in coastal areas during red tides of harmful algae can bring pathogens in the atmosphere as aerosols, causing health issues [20,21]. Control of jet drops sizes and velocity has also been a subject of interest with application to the sparkling wine industry [22,23].

*ldeike@princeton.edu

 ©2018 American Physical Society

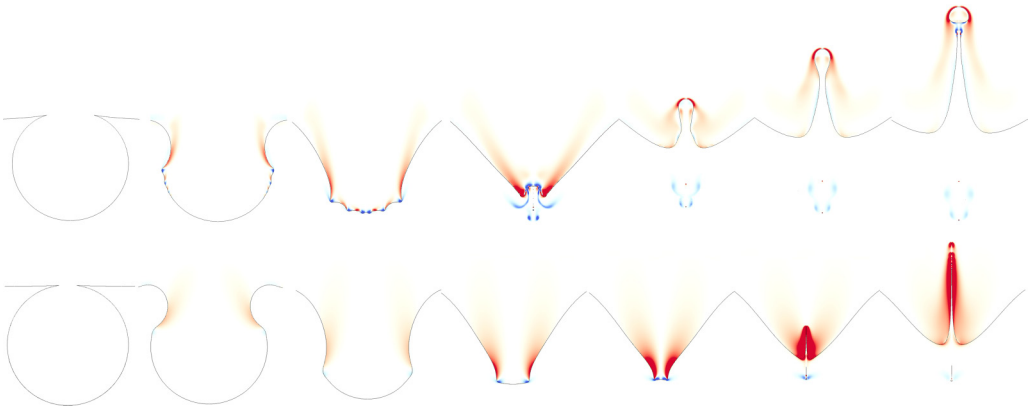

FIG. 1. Direct numerical simulations of the axisymmetric Navier-Stokes equations, using Gerris, of a bursting bubble and subsequent jet formation. Top: Bond number Bo $= 0.1172$, and Laplace number La $= 6.7 \times 10^4$, or Morton number Mo $= 2.63 \times 10^{-11}$ corresponding to a bubble radius $R_0 = 934$ μm in water. Several fast capillaries propagate toward the center of the cavity, with significant vorticity being generated, and leading to the creation of a jet, that then pinches off to release droplets. Times of the snapshots are $t/t_{\text{ic}} = 0$, 0.16, 0.32, 0.40, 0.48, 0.54, and 0.60. Bottom: bursting close to the optimal Laplace number, with bond number Bo $= 0.01$, and Laplace number La $= 10^3$. During the cavity collapse, a single capillary wave is seen propagating toward the center with relatively low vorticity being generated before focusing. The collapse can be described by a self-similar dynamics and gets close to the finite-time singularity. At focusing, a very strong vorticity field is observed, associated with a very thin and fast jet, small drops being quickly ejected. Times of the snapshots are $t/t_{\text{ic}} = 0$, 0.16, 0.32, 0.43, 0.45, 0.46, and 0.48. The color field represents vorticity Γ in the gas and liquid (with maximum vorticity in red, $\Gamma t_{\text{ic}} = 190$, and minimum in blue $\Gamma t_{\text{ic}} = -190$). Maximum refinement corresponds to a grid equivalent to $(2^{13})^2$, corresponding to 1638 grid points per bubble diameter.

Since the pioneering study of bursting bubbles published by Woodcock *et al.* in 1953 [24], the past 65 years have witnessed a number of studies documenting jet drop properties; however, the fundamental mechanism leading to the ejection of jet drops is still unclear. The first comprehensive study, realized by Duchemin *et al.* [17] using numerical simulations based on a free-surface formulation of the Navier-Stokes equations, showed that fast jets are produced by the self-similar collapse of a cavity created by focusing capillary waves. The cavity collapse leading to the jetting dynamics can be described by a self-similar dynamic based on the balance of inertia and capillarity [25,26]. This leads to a singular behavior where the velocity diverges. The singularity is in practice regularized by viscous and capillary effects. Viscosity was shown to play a crucial role in the control of this focusing. Counterintuitively, the fastest jets are not obtained for a vanishing viscosity, rather they occur in a relatively narrow range of optimal viscosity : for a Laplace number La $= \gamma R_0 \rho/\mu^2$ around 1000, with R_0 the bubble radius and γ, ρ, and μ, respectively, the surface tension, density, and viscosity of the liquid. For this particular value the system approaches a finite-time singularity, where the curvature and subsequently the pressure and the velocity tend to diverge [25,26].

An explanation of this phenomenon is that the damping action of viscosity shelters the self-similar collapse from short wavelength capillary perturbations, allowing it to come closer to the singular limit and therefore produce faster and smaller droplets. Earlier numerical simulations of the phenomenon relied on boundary integral methods for an inviscid fluid [27–30] and thus missed this important mechanism. Full Navier-Stokes simulations have recently been presented and focused on the range of existence of jet drops [31]. A theoretical study has just been published [32] based on a balance between viscosity, inertia, and surface tension during the curvature reversal leading to the jet formation (neglecting gravity, thus valid for small Bond numbers, Bo $\ll 1$).

However, several aspects of the phenomenon were not addressed in Duchemin *et al.* [17]. In particular, the effects of gravity were not taken into account. As a consequence a simplified initial

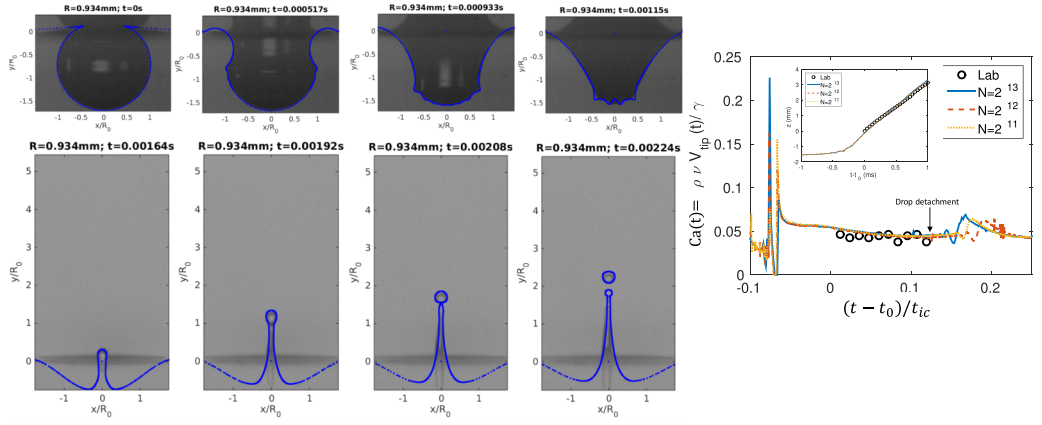

FIG. 2. Jet dynamics of a bursting bubble in water, bubble radius is $R_0 = 934\ \mu$m. Bond number Bo $=$ 0.1172, Laplace number La $= 6.7 \times 10^4$, or Morton number Mo $= 2.63 \times 10^{-11}$. Left: Experimental time sequences superposed with numerical profiles. The top four panels show the event below the free surface, while the bottom four panels display the bubble above the free surface. The top four panels take place before the first image of the bottom panels. Excellent agreement between the numerical and experimental data is observed for the cavity collapse dynamics, as well as for the jet formation and the first ejected droplet. Differences appear for the dynamics of the jet after the first drop is ejected and for the following satellite drops. Right: Time evolution of the vertical velocity of the apex of the cavity, becoming the tip of the jet, $\mathrm{Ca}(t) = [\rho\nu V_{\mathrm{tip}}(t)]/\gamma$. Time is shifted by t_0, the time at which the jet crosses the $z = 0$ reference point and normalized by t_{ic}. Black circles are laboratory data from Ref. [7], while color lines are DNS with increasing resolutions (from 2^{11} to 2^{13} equivalent grid size). Excellent agreement is observed between the laboratory and numerical results, as well as mesh convergence. The velocity of the jet is still decreasing when it crosses the $z = 0$ horizontal line, and it reaches a constant value before the formation of the first drop, which we define as V_{tip}. The first drop detachment is indicated with an arrow. Inset: same data for the vertical position of the central point of the cavity, becoming the tip of the jet.

condition was used: a spherical bubble exactly tangent to a flat surface with a very small hole at the top. This can indeed be seen as the limiting case where surface tension effects are much larger than gravity effects. Furthermore, only limited and qualitative comparisons with experiments were made, mostly due to the scarcity of quantitative experimental data available at the time. In this context, the present article has two primary aims: (1) verify that experimental and numerical results are indeed quantitatively consistent across the entire range of accessible parameters (and clarify the theoretical assumptions necessary to obtain such an agreement), (2) obtain a complete quantitative description of the dependence of the jet velocity on both viscosity and gravity, and properly separate these two effects.

This article presents a full cross-validation of numerical and experimental results for this problem and includes high-resolution, high-fidelity direct numerical simulations of the full two-phase flow problem. In particular, the convergence of the results close to the singular limit is discussed and the shape of the collapsing cavity, and its velocity are analyzed and compared in detail with experiments. The dependency on the Bond number (effect of gravity relative to surface tension) is studied systematically using numerical simulations, significantly increasing the range of parameters covered experimentally. This unique data set allows us to propose a universal relationship for the jet velocity.

The article is organized as follows. In Sec. II, we present the numerical techniques, experimental results used for comparisons, relevant nondimensional numbers, as well as examples of the cavity collapse, jet formation, and drop generation. Experimental and numerical cavity collapse are cross validated and we discuss the definition of the jet velocity by comparing laboratory and numerical data. In Sec. III, we explore numerically a wide parameter space in terms of nondimensional numbers:

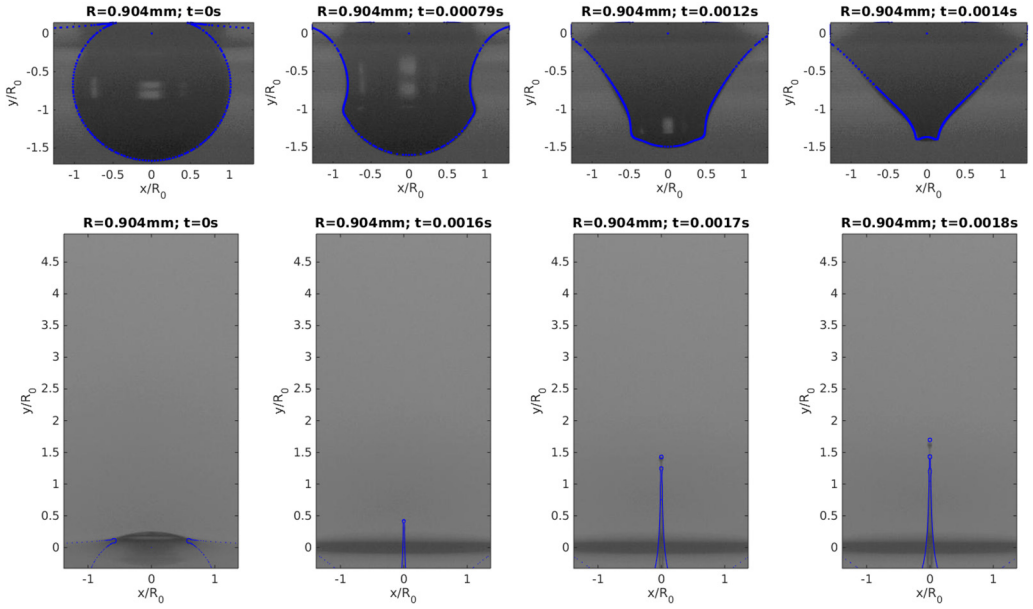

FIG. 3. Experimental time sequences superposed with numerical profiles of a typical jetting event following a bubble bursting at a free surface of silicon oil. The top four panels show the event as seen from above the free surface, while the bottom four panels display the bubble under the free surface. The bottom three right panels take place between the first two images of the top panels. Bubble radius is $R_0 = 904$ μm. Bond number Bo $= 0.14$, Laplace number La $= 1697$, or Morton number Mo $= 4.86 \times 10^{-8}$. A single capillary wave propagates towards the center of the cavity, creating a sharp corner and leading to a very thin jet, corresponding to the optimal Laplace number and a dynamic close to the finite-time singularity. Very good agreement between experimental and numerical profiles is observed up to the formation of the first drop. The jet velocity V_{tip} is defined as the velocity before drop ejection.

the Laplace number (viscous relative to inertia) and the Bond number (gravity relative to capillary forces). We then discuss the influence of the capillary wavelength on the jet velocity. The crucial role played by the initial cavity shape on the final jet velocity, through the selection of different wavelengths capillary waves, is detailed in the Appendix. We present a universal scaling for the jet tip velocity formed by bursting bubbles, as a function of the Laplace and Bond numbers. Finally, we compare our numerical results with recent theoretical work [32]. The theory from Gañán-Calvo [32] is restricted to small Bond numbers (Bo $\ll 1$), neglecting the effect of gravity. We extend this work to finite Bond numbers and show how the theoretical scaling for the jet velocity can be adapted to account for the influence of gravity.

II. EXPERIMENTAL CONFIGURATION AND NUMERICAL SIMULATION

A. Experimental and numerical setup, nondimensional numbers

The experiments have been described in detail in Ghabache *et al.* [7,18,33] and consist in releasing a gas bubble from a submerged needle in a bulk liquid and recording the upward jet after the bubble bursts at the free surface. The bubble radius, selected by imposing the needle diameter, ranges from 300 μm to 5 mm, and the liquids used include water-glycerol-ethanol mixtures with varying viscosity, surface tension, and density. The bubble collapse and jet dynamics are analyzed through fast and close-up imagery using a digital high-speed camera and zoom lens systems. The spatial resolution is typically 5 μm per pixel and the acquisition rate between 10 000 and 150 000 frames per second.

As described in Refs. [7,15], when the cavity collapse starts (just after bursting of the film), the cavity presents the static shape of the bubble at the gas-liquid interface. This can be obtained theoretically by solving the Young-Laplace equations [15,34], assuming that surface tension is constant and the bubble is shaped by the competition of surface tension and gravity. For each bubble cavity of radius R_0 (or in a nondimensional way, for a given Bond number) we have to compute the static bubble profile, which has been shown to accurately describe the shape of the bubble cavity after the initial film break-up, right before the cavity left by the bubble starts to collapse [7,15].

The numerical simulations are performed by solving the axisymmetric, two-phase, incompressible Navier-Stokes equations with surface tension using the open source solver Gerris [35,36], based on a quad/octree adaptive spatial discretization and a multilevel Poisson solver. The interface between the high density liquid and the low density gas (air) is reconstructed by a volume of fluid (VOF) method and an accurate, well-balanced surface-tension model is used. The Gerris flow solver has been extensively used and validated for complex multiphase problems, such as atomization [37,38], the growth of instabilities at the interface [39], wave breaking in two and three dimensions [9,37,40,41], capillary wave turbulence [42], and splashing [43,44]. Here, we use the adaptive mesh of Gerris to solve the collapsing dynamics at very high resolution, with a grid size up to an equivalent of 8192^2 (corresponding to 1638 grid points per bubble diameter), which is necessary to obtain numerically converged results, especially for the very narrow and high-speed jets. The ejection velocity of the jet and the resulting droplets can then be analyzed and compared to the experimental results.

The physical parameters of the problem are the bubble radius R_0, liquid density ρ, dynamic viscosity μ, surface tension γ, and gravity g. The density of the gas is set to $\rho_g = 10^{-3}\rho$, while the viscosity of the gas is set to $\mu_g = 10^{-2}\mu$, meaning that we are working at high density and viscosity ratio. In this context the gas is supposed to have no influence on the dynamics of the cavity collapse and jet formation.

We initialize the liquid-gas interface with the theoretical shape of the cavity left by a bursting bubble of radius R_0. The initial condition of the simulation is therefore a close match to the experimental one. We will show later that the details of the cavity shape participate in selecting the capillary waves generated during the cavity collapse and therefore strongly influence the jet velocity. Consistent comparisons with laboratory experiments thus require that the capillary/gravity equilibrium bubble shape be used as initial condition. Note that we do not attempt to resolve numerically the break-up of the initial film (the bubble cap) but start the simulation directly with the opened cavity.

This system is therefore fully described by only two dimensionless numbers, for example, the Bond number Bo (ratio between gravity and capillary forces), and the Laplace number La (ratio between inertiocapillary and viscous effects, effectively similar to a Reynolds number):

$$\begin{aligned} \mathrm{Bo} &= \frac{\rho g R_0^2}{\gamma}, \\ \mathrm{La} &= \frac{\rho \gamma R_0}{\mu^2}. \end{aligned} \tag{1}$$

We choose as characteristic length and time scales of the problem, the bubble radius R_0 and the inertiocapillary time scale $t_{\mathrm{ic}} = \sqrt{\rho R_0^3/\gamma}$, equivalent to the frequency of a capillary wave with wave number $k = 1/R_0$. As in the experimental study of Ghabache *et al.* [7], we can also work with the Morton number, instead of the Laplace or Bond number, with the definition:

$$\mathrm{Mo} = \frac{g\mu^4}{\rho\gamma^3} = \mathrm{BoLa}^{-2}. \tag{2}$$

The Morton number has the advantage of being constant for a given fluid; however, it has the disadvantage of being harder to interpret as it "mixes" all parameters/effects, in contrast with the Bond and Laplace numbers, which can simply be interpreted as the nondimensional gravity and

inverse of viscosity (i.e., a Reynolds number), respectively. Note that instead of the Laplace number, the Ohnesorge number can also be used, $\mathrm{Oh} = \mathrm{La}^{-1/2}$, as in Walls *et al.* [31]. Experimentally, Ghabache *et al.* [7] defined an effective bubble radius based on an elliptic fit and the two axis of the fitted ellipse, R_{eff}. We have verified that using R_{eff} or R_0 leads to differences in the characteristic nondimensional number of less than 1%. These differences are well below the experimental or numerical uncertainties.

The primary measurement is the velocity of the jet V_{tip}, we will discuss its definition in Sec. III. Earlier numerical studies have defined V_{tip} as the instantaneous velocity when the jet crosses the $z = 0$ horizontal line [17]. Experimentally, Ghabache *et al.* [7] measured the averaged jet velocity over the first few images after it passes the $z = 0$ horizontal line. We will see that these two velocities are not necessarily equal since the jet velocity can still be decreasing when it passes $z = 0$. This difference in definition can lead to biases when comparing experimental and numerical results and also when comparing results from different groups. Here, the jet velocity is measured as it reaches a stationary state, usually just before the first drop detaches from the jet, which is consistent with experimental measurements [7]. This velocity is then directly related to the top drop ejection velocity. Since we analyze the jet tip velocity, we define nondimensional numbers related to this velocity, for example, the Weber number:

$$\mathrm{We} = \frac{\rho V_{\mathrm{tip}}^2 R_0}{\gamma}, \tag{3}$$

which compares inertial effects and surface tension, or the capillary number:

$$\mathrm{Ca} = \frac{\mu V_{\mathrm{tip}}}{\gamma}, \tag{4}$$

which compares the jet velocity with the viscocapillary velocity σ/μ. One of the goals of the paper is to provide a master curve for a nondimensional tip velocity as a function of the Bond and Laplace numbers.

Solving the small-scale features of the collapsing cavity and the emerging jet is a challenging numerical task, requiring very high resolution. As already mentioned, we use the adaptive feature of Gerris with meshes equivalent to at least $2^{11} \times 2^{11}$ and up to $2^{13} \times 2^{13}$ grid points. All results presented in the papers are converged with respect to the mesh size, i.e., results do not change if the resolution is increased. The numerical convergence of the jet velocity was verified for the entire range of Laplace numbers. The resolution necessary to reach convergence depends mostly on the Laplace number. If the Laplace number is around 1000, i.e., the dynamics get close to the finite-time singularity, then convergence is observed for a resolution between 2^{12} and 2^{13}, while for higher Laplace numbers, typically for $\mathrm{La} > 3000$, mesh convergence is observed for resolutions between 2^{11} and 2^{12}. Finally, the results are carefully validated against laboratory data [7] for a wide range of Laplace and Bond numbers.

B. Cavity collapse and jet formation: Numerical and experimental validation

Figure 1 illustrates direct numerical simulations of two typical jetting events following a bubble bursting at a free surface. The top panels illustrate a case in water, for a large Laplace number (radius in water is $R_0 = 934$ μm corresponding to a Bond number $\mathrm{Bo} = 0.1172$, a Laplace number $\mathrm{La} = 6.7 \times 10^4$, or Morton number $\mathrm{Mo} = 2.63 \times 10^{-11}$). We see a train of capillary waves propagating along the cavity, associated with a significant vorticity generation [40], and focusing at the bottom. These collapsing waves focus at the center of the cavity and give rise to a high-speed vertical jet shooting out above the free surface as observed in the top sequence. The jet then fragments into droplets generating an aerosol of $O(10)$ droplets [3,33,34]. During the focusing, the different capillaries arrive to the center of the cavity at different times, leading to very fast oscillations of the bottom of the cavity before the jet is formed and ejected. Entrainment of small gas bubble back into the liquid pool is visible.

The bottom panels illustrate a case close to the optimal Laplace number $\mathrm{La} = 10^3$ and $\mathrm{Bo} = 0.01$. While a similar dynamic as in water is observed, we also see important differences. The train of capillary waves is damped by the higher viscosity and only a single capillary wave is propagating toward the center of the cavity, with weaker vorticity generation before reaching the center of the cavity. It leads to the creation of a sharp corner, and a dynamic getting very close to the finite-time singularity with very strong vorticity field and the generation of a much faster and thinner jet. Several drops are formed when the thin and fast jet moves upward. Entrainment of small gas bubbles back into the liquid pool is also visible.

Figure 2 (panels on the left) illustrates a typical jetting event following a bubble bursting at a free surface in water (same case as in Fig. 1). The bottom sequence shows the free surface view while the top one displays the underwater dynamics. The first image of the bottom sequence shows a static bubble lying at the free surface. The film separating the bubble from the atmosphere drains and bursts leaving an unstable opened cavity. The top sequence displays a train of capillary waves propagating along the cavity and focusing at the bottom. The computed cavity and jet profiles have been superimposed on both experimental sequences. Agreement between the experimental and computed profiles is very good for the cavity collapse, the formation of the capillary waves on the cavity, the jet formation and up to the detachment of the first drop. The size and velocity of the first drop are very well captured in the simulation while the subsequent drops differ between the laboratory and numerical data.

Figure 2 (right) shows both the numerical and experimental time evolution of the vertical velocity (and position in inset) of the central point of the cavity, which becomes the tip of the jet once it is formed, for this bubble in water ($\mathrm{Bo} = 0.1172$, $\mathrm{La} = 6.7 \times 10^4$). The time t_0 corresponds to the moment when the tip of the jet crosses the $z = 0$ position, i.e., the beginning of the experimental recording of the jet. The time evolution is shown for different grid resolutions and one can see that convergence is reached with only very small variations between the different grids. At $(t - t_0)/t_{\mathrm{ic}} \approx 0.15$, the first drop is ejected, and after that time, some differences between the different resolutions are observed. The slight bump in velocity corresponds to oscillations of the detached drop. The numerical results are in excellent agreement with the experimental data [7], given the complexity of both the experiments and the numerical simulations.

The vertical velocity of the apex of the cavity increases very rapidly when the capillary waves focus, and experiences rapid oscillations during the time the small ripples are reaching the apex and give rise to a vertical jet. Interestingly, we will see that close to the singularity, these oscillations are not present, since focusing does not involve a train of waves but a single one. The vertical jet reaches its maximal velocity just after formation, and the velocity then decreases to reach a constant value before the first droplet ejection. It is clear that when the jet crosses the $z = 0$ mean water level, its velocity is still decreasing and therefore measuring the instantaneous jet velocity at this instant is not physically meaningful, since it is still in a transient regime.

We therefore consider that the relevant jet tip velocity is the plateau value reached before drop ejection and we define it as the jet velocity V_{tip}. This value is the one that is effectively measured experimentally when defining an average velocity over the first few images after the jet crosses $z = 0$. Consequently, we only define V_{tip} for jets that create a drop, and we will discuss the range of parameters (Bond and Laplace numbers) for which drop ejection is observed.

Making this distinction between the jet velocity at $z = 0$ and V_{tip} as defined here is crucial for obtaining consistent results between the experimental and numerical datasets. For some regimes, such as intermediate Laplace numbers $4000 < \mathrm{La} < 40\,000$, these two values are identical, since the $z = 0$ crossing coincides with the plateau velocity, but for lower and larger Laplace numbers, this distinction must be made. This discussion on the definition of the tip velocity has to be remembered when comparing results in the literature, both from numerical simulations and laboratory experiments.

Figure 3 illustrates a jetting event at the free surface of a more viscous liquid. This case is similar to the one close to the optimal Laplace number presented in Fig. 1, with a bubble radius of $R_0 = 904\ \mu\mathrm{m}$, corresponding to a Bond number of $\mathrm{Bo} = 0.14$ and Laplace number $\mathrm{La} = 1697$. The train of capillary waves is replaced by a single capillary wave propagating toward the center of

the cavity, leading to the creation of a sharp corner and the generation of a much faster and thinner jet. The cavity dynamics, as well as the jet formation and first-drop generation, are again very well captured by the numerical simulations.

Similar comparisons can be made for the whole range of Laplace and Bond numbers tested. The simulations capture very well the collapse of the cavity, together with the jet formation and the first drop, while departure is observed for the generation of satellite droplets. These differences are not surprising since, even in experiments, the size of the second drop can take two different values (Spiel's bimode), whereas the size of the first drop is very well defined and unique [33,34]. This is happening when what seems to be the future second and third drops are not able to separate properly. In this case, we get either a big second drop (no separation) or a small second drop (good separation). This process is not well understood but might be related to small asymmetries during the bubble collapse, responsible for not perfectly vertical jets and then variability in the pinch-off dynamic. In light of that discussion, simulations give access to the ideal case of perfectly vertical and axisymmetric jets that are very difficult to achieve in laboratory experiments, whereas experiments give an overview of what happens in nature with nonperfect axisymmetric conditions.

III. JET DYNAMICS

A. The emerging jet and the tip velocity

Let us first give more details on the time evolution of the jet velocity as a function of the relevant parameters to grasp the influence of each effect before we present a systematic study. Four regimes are identified in terms of the Laplace number: at low Laplace numbers, $\mathrm{La} < 500$, no drop is formed and we do not define the jet velocity, at intermediate Laplace numbers $500 \leqslant \mathrm{La} \leqslant 1000$, drops are formed and the velocity increases, at high Laplace number $\mathrm{La} > 1000$, drops are formed and the jet velocity decreases as the Laplace number increases. An optimum is reached for $\mathrm{La} \approx 1000$ with very thin and fast jets. Figure 4 shows the jet capillary number Ca as a function of time for three Laplace numbers (500, 1000, and 10^4) and three different Bond numbers (0.1, 0.01, and 0.001) in each case, together with the time evolution of the cavity and the jet formation for a single Bond number ($\mathrm{Bo} = 0.01$).

At high Laplace number ($\mathrm{La} = 10^4$), Figs. 4(a) and 4(b) show that the velocity of the center of the cavity increases abruptly when the first capillary wave focuses at the center of the cavity. The peak capillary velocity Ca of the apex for the three Bond numbers is lower than unity. Two main capillary waves are observed, arriving at different times at the center of the cavity, before the jet forms. The jet is relatively thick and eventually pinches off to form a drop. The jet reaches a well-defined stationary velocity before the first drop is formed, which we define as the tip velocity V_{tip}. This case is similar to the one presented for water in Fig. 2(a), which was also for a high Laplace number. The time of the first drop generation is indicated on Fig. 4(b) by an arrow for each simulation. The jet velocity decreases when increasing the Bond number, and we observe a delay in the drop formation related to this lower velocity. The lower velocity can be related to the wavelength of the capillary wave generated when the cavity starts collapsing, with longer wavelength being selected by the initial condition, due to the effect of gravity on the initial bubble static shape. This longer wavelength leads to the lower velocities as suggested by the dispersion relation of gravity-capillary waves in deep-water $c = \sqrt{g/k + \gamma k/\rho}$.

At low Laplace number ($\mathrm{La} = 500$), Figs. 4(c) and 4(d) show that the apex velocity also increases abruptly when the capillary wave focuses at the center, and then continuously decreases, with no drop formation. Only one capillary wave is visible in this case, the smaller capillaries being damped by viscosity. This leads to a cleaner focusing and a higher velocity at the center of the cavity than in the high Laplace number case because of a more efficient focusing of the available energy in a smaller cavity. In this case, no drop formation is observed. When the jet moves upward, transverse oscillations in the jet lead to some oscillations in the velocity, but are not strong enough to lead to drop detachment, probably due to the strong viscous effects. These oscillations are related to capillary waves and the pinching is avoided in a process that appears similar to the one described in Hoepffner

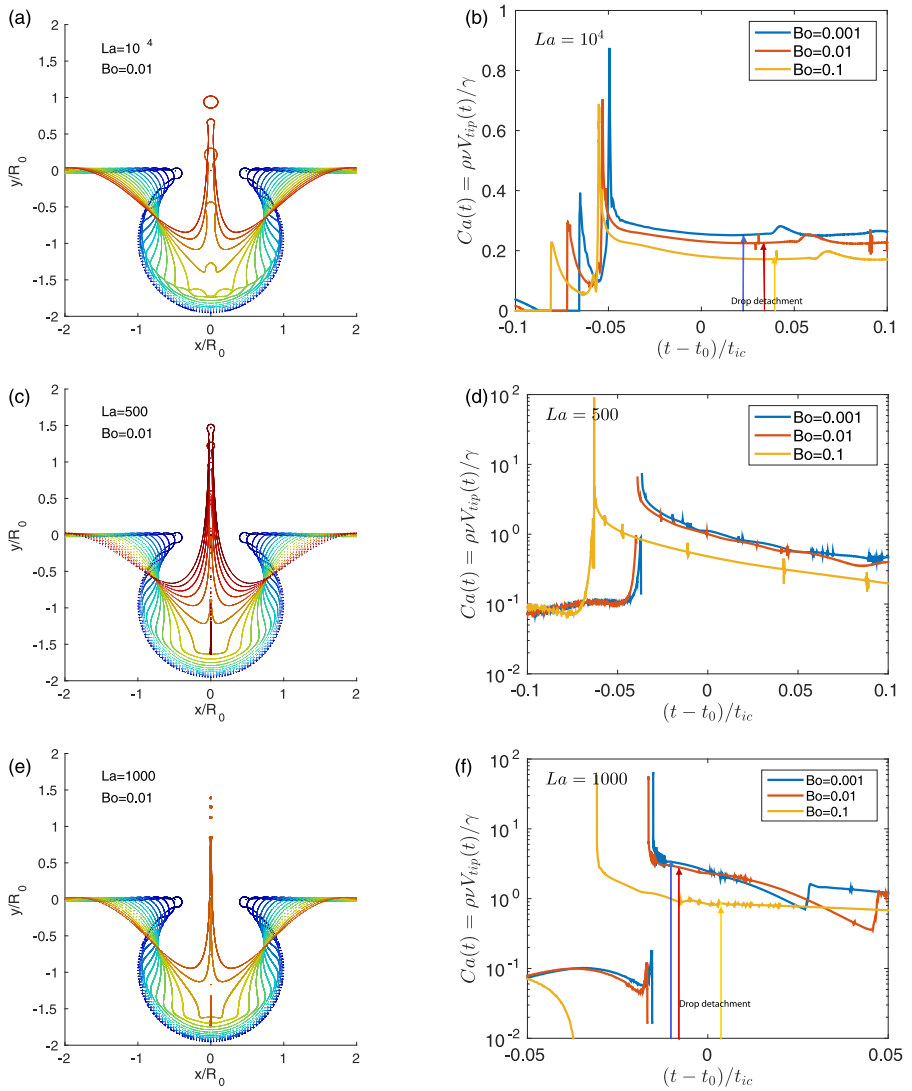

FIG. 4. Left panels (a, c, e) Time evolution of the cavity profile, showing the collapse and jet formation for three Laplace numbers, at Bo = 0.01. Time is color coded and increases from blue to red, with $\Delta t = 0.03 t_{\rm ic}$ between each profile. (a) La = 10^4: several capillary waves are seen propagating toward the center, creating a jet that eventually pinches off and forms drops. No air bubble entrainment is observed. (c) La = 500: a single capillary wave is visible propagating toward the center of the cavity, leading to a thinner jet, which does not pinch off. Air entrainment in the liquid is observed when the jet is formed. (e) La = 1000, the self-similar collapse comes very close to a finite time singularity, with a single capillary wave focusing to the center of the cavity, leading to a very fast and thin jet, which pinches off quickly and forms drops. Air entrainment is observed when the jet is formed. Right panels (b, d, f) Time evolution of the vertical velocity of the apex of the cavity, becoming the tip of the jet Ca$(t) = [\rho \nu V_{\rm tip}(t)]/\gamma$, for three different Laplace numbers and three Bond numbers, representative of the dynamics at high Laplace number (La = 10^4), low Laplace number with no drop formation (La = 500), and Laplace number close to the capillary singularity (La = 1000). Time is normalized, $(t - t_0)/t_{\rm ic}$. For each case, the velocity for three Bond numbers is shown (Bo = 0.1, Bo = 0.01, Bo = 0.001), with the velocity decreasing when increasing the Bond number. (f) La = 1000, the dynamic is close to the finite time singularity for the smallest Bond numbers, while the velocity of the jet is much smaller in the Bo = 0.1 case, due to gravity effects on the shape of the cavity. Arrows indicate the time just before drop formation.

and Paré [45]. Also, we observe the entrainment of small air bubbles, which might take significant energy out of the jet, participating in preventing drop ejection. The jet velocity decreases until it gets back to zero (not shown). In some cases a drop can detach during the fall back of the jet, with a much smaller velocity than that of an ejected drop, before quickly falling back into the bath. The velocity is smaller for higher Bond numbers, which is again attributed to the effect of gravity on the cavity shape. We do not define a jet tip velocity in these cases where no drop is generated during the upward motion of the jet.

Finally, one of the most interesting case is close to the optimal Laplace number, $\mathrm{La} = 1000$ [Figs. 4(e) and 4(f)]. The dynamics are initially similar to the low Laplace number case, with a single wave propagating towards the cavity apex, but when the capillary wave focus to the cavity center, the jet reaches a much higher normalized velocity, up to $\mathrm{Ca}(t) \approx 200$. The cavity presents a singular square shape with dynamics well-described by a self-similar capillary scaling and a dynamic getting close to a finite-time singularity [7,17,26]. A very thin and very fast jet is formed and its velocity decreases very quickly before the first drop detaches. The plateau velocity of the apex just before drop detachment, observed for a very short time, is taken as the tip velocity, and the time at which the first drop detaches is indicated by arrows in Fig. 4(f). This quasisingular behavior is observed for the two lowest Bond numbers (red and blue curves), with a jet velocity slightly higher for the lowest Bond number. For the higher Bond number ($\mathrm{Bo} = 0.1$), the focusing is affected by gravity effects and is less efficient, and the dynamics does not get as close to the finite time singularity as before, the earlier regularization leading to a significantly smaller jet velocity, due to the change in the cavity shape by gravity effects. This result shows that both the Bond and Laplace numbers are necessary to describe the singular dynamics of the jet, thus considering viscous, inertial, capillary, and gravity effects.

In all cases, the tip velocity is maximum at the formation of the jet, when the capillary waves have focused. This maximal velocity is highly dependent on the details of the focusing process. The velocity of the apex at the center of the cavity then decays before reaching a plateau value just before drop ejection. This velocity is defined as the tip velocity V_{tip} and is physically relevant since it is related to the drop velocity. At low Laplace numbers, the velocity decreases continuously due to strong viscous effects, without drop formation.

B. A systematic study

We now perform a systematic study in the (La,Bo) parameter space and extract the tip velocity V_{tip} as described previously. First, we present an extensive comparison-validation of the numerical results with laboratory data. We match and extend experimental conditions presented in Ghabache *et al.* [7] and work with five different Morton numbers while varying the Bond number over a wide range. We then perform numerical simulations for a systematic parameter sweep in terms of Laplace La and Bond Bo numbers.

Figure 5(a) shows the parameter space diagram (La,Bo) for which drop ejection is observed. Color symbols correspond to runs at constant Morton number, each color representing a working liquid. We vary the Bond number and by definition $\mathrm{La} = (\mathrm{Bo}/\mathrm{Mo})^{1/2}$. Black symbols correspond to a systematic sweep in the (Bo,La) space. A critical value of $\mathrm{La}_c = 500$ is found below which no drop formation is observed during the upward rise of the jet. Below this critical value, drop ejection is prevented by viscous effects. This result is close to the one described by Walls *et al.* [31], which found a critical Ohnesorge number of $\mathrm{Oh}_c \approx 0.04$, which corresponds to $\mathrm{La}_c = \mathrm{Oh}_c^{-2} \approx 650$. As described in Refs. [7,31], for higher Bond numbers, gravity has a key influence on the jet velocity and participates in preventing drop formation, and we see that the boundary between drop ejection and no drop ejection depends on the Bond number, for $\mathrm{Bo} > 0.05$. An empirical boundary is traced on the figure, describing the observed parameter space of drop ejection, $\mathrm{La}_c(\mathrm{Bo} > 0.05) \propto \mathrm{Bo}^{2/3}$ and equivalent to the one presented by Walls *et al.* [31], $\mathrm{Oh}_c \propto \mathrm{Bo}^{-1/3}$ in the same regime of Bond number.

Figure 5(b) shows the jet capillary number Ca as a function of the Bond number for experiments (solid circles) and numerical simulations in water ($\mathrm{Mo} = 2.63 \times 10^{-11}$) (open symbols) for the four

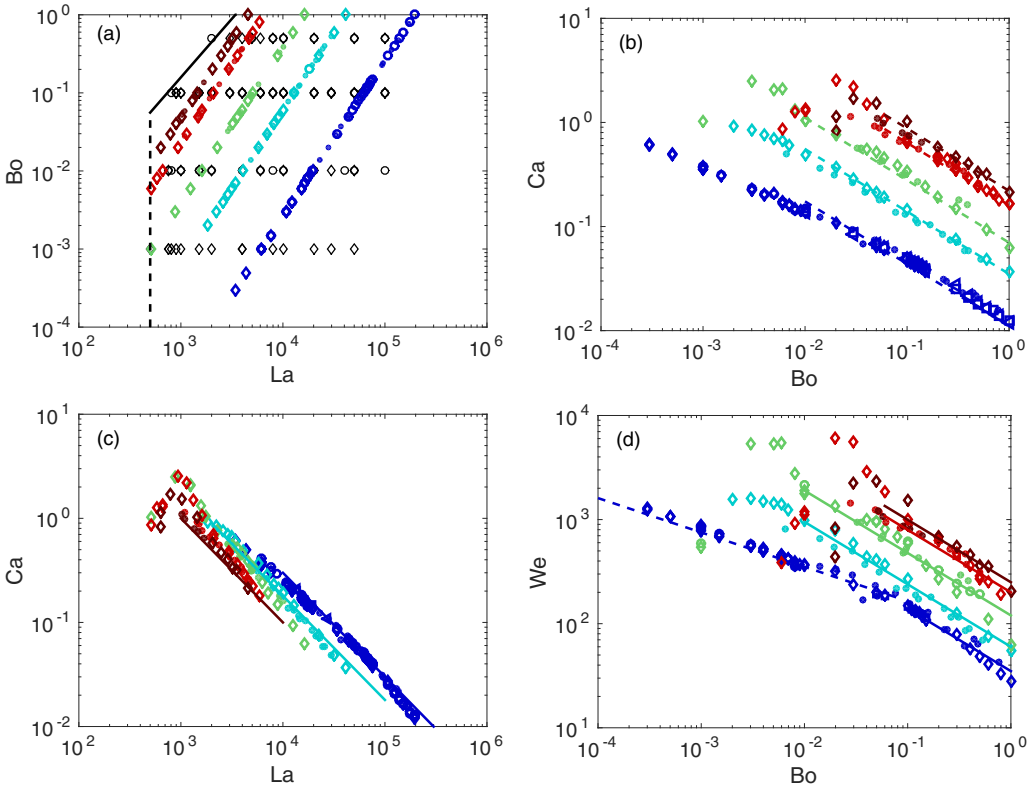

FIG. 5. Color symbols are the runs at a constant Mo (and by definition $\mathrm{La} = (\mathrm{Bo}/\mathrm{Mo})^{1/2}$). Each color is a different liquid with increasing Morton number: blue, $\mathrm{Mo} = 2.63 \times 10^{-11}$ (water), light blue $\mathrm{Mo} = 5.99 \times 10^{-10}$, green $\mathrm{Mo} = 3.2 \times 10^{-9}$, light red $\mathrm{Mo} = 2.3 \times 10^{-8}$, and dark red $\mathrm{Mo} = 4.8 \times 10^{-8}$. DNS are open symbols (diamond and circles are 2^{12} and 2^{11} mesh size, respectively) and solid dots are experimental data. Mesh convergence is observed as well as good agreement between DNS and laboratory data. (a) Parameter space (La, Bo) where drop formation is observed in the numerical simulations and experiments, with at least one drop ejected by the ascending jet. Black symbols are from the (Bo, La) sweep. The black dashed line indicates a critical Laplace number below which no drop ejection is observed, $\mathrm{La}_c = 500$. The solid black line is the boundary between the regimes with and without drop ejection, $\mathrm{Bo} \propto \mathrm{La}^{3/2}$. (b) Jet capillary number $\mathrm{Ca} = V_{\mathrm{tip}}\mu/\gamma$ as a function of the Bond number. Dashed lines are $\mathrm{Ca} \propto \mathrm{Bo}^{-0.6}$ relationships for each working liquid, observed at high Bo while a change of regime, or saturation of the capillary velocity is observed at lower Bo. (c) Jet capillary number Ca as a function of La. The singularity is observed around $\mathrm{La} \approx 1000$. At a given Laplace number, the jet capillary number decreases when increasing the Morton number, due to Bond number effects. Very good agreement is found between numerical and experimental data except near the singularity $\mathrm{La} \approx 1000$, where some differences are visible due to the very high velocity of the jet. Solid lines are $\mathrm{Ca} \propto \mathrm{La}^{-1}$ relationships for each working liquid, observed at high La. (d) We as a function of Bo. Solid lines are $\mathrm{We} \propto \mathrm{Bo}^{-0.6}$ relationships for each working liquid at high Bond number and dashed line is $\mathrm{We} \propto \mathrm{Bo}^{-0.33}$ at low Bond number for water. The value of the We seems to saturate, for a given liquid, to a constant value and a $\mathrm{We} \propto \mathrm{Bo}^{0}$.

working fluids. Numerical convergence is reached and excellent agreement between the laboratory and numerical data is observed. If the Morton number is kept constant (i.e., same working liquid), the Bond number can only vary if the bubble diameter varies. We therefore observe that velocity decreases as the bubble radius increases. Moreover, the numerical study highly extends the range of Bond numbers investigated experimentally for the smallest bubbles. Here the smallest Bond number is 2×10^{-4}, which corresponds to a bubble radius of 38 microns in water while in Ghabache *et al.* [7]

the smallest Bond was 10^{-2} and corresponds to a bubble radius of 270 microns in water. Finally, we observe that for Bo > 0.01 in all liquids, the jet velocity scales like Ca $\propto$ Bo$^{0.6}$, while a change of slope for Bo < 0.01 is visible in the case of lower viscosity, and a saturation can be seen for the higher viscosity.

Figure 5(c) shows the capillary versus Laplace number. As already described in Duchemin *et al.* [17], and confirmed experimentally in Ghabache *et al.* [7], the primary control on the jet velocity is the viscosity (i.e., Laplace number). Viscous damping of high-frequency capillary waves improves the focusing of the primary wavelength (comparable to the size of the initial cavity) and leads to a thinner and faster jet. If the viscosity is too high however, the jet velocity decreases due to high shear, high vorticity generation and extra viscous damping of the focusing waves. Eventually, drop formation is entirely suppressed by viscosity (for La < 500 in Fig. 5(c)). An optimum is reached for Laplace numbers of order 1000 corresponding to the near singular collapse studied by Duchemin *et al.* [17]. Note that this regime is only reached experimentally for the most viscous liquids (red and green symbols). The influence of gravity is best analyzed through the Bond number dependence and will be discussed in detail later in the article. At this stage it is sufficient to note that increasing Bond numbers are related to increasing Morton numbers, so that the datasets in Fig. 5(c) are roughly ordered in increasing Bond number from dark blue to dark red. The primary influence of the Bond number (i.e., gravity) is thus a downward shift of a master distribution, which itself depends primarily on the Laplace number. Note that we observe small differences between numerical and laboratory data near the singularity, which might be attributed to the very high jet velocity and thin jets, leading to higher uncertainties in both the experimental measurements and the numerical simulations. For all Morton numbers, a decay at high Laplace number Ca $\propto$ La^{-1} is observed.

Figure 5(d) shows the Weber number versus the Bond number, it is similar to Fig. 5(b). For Bo > 0.1 we see a We $\propto$ Bo$^{-0.6}$ scaling in water (dark blue), similar to the We $\propto$ Bo$^{-0.5}$ scaling reported in Ghabache *et al.* [7]. A change of slope is observed at smaller Bond number, with We $\propto$ Bo$^{-0.33}$ for $10^{-4} <$ Bo < 0.1. This change of slope is visible because the numerical simulations have widely extended the range of parameters. However, even with such low Bond number, the jet velocity remains influenced by gravity and does not reach the pure inertiocapillary velocity, characterized by a constant Weber number. This surprising result is at variance with the recent discussion of Krishnan *et al.* [46]. When the viscosity is increased (light blue), we observe the same scaling We $\propto$ Bo$^{-0.6}$ for Bo > 0.01 as in water, consistent with Ghabache *et al.* [7]. In this case, a saturation is reached at lower Bond number, i.e., a regime where We $\sim$ Bo^0, gravity has lost its influence. For higher viscosity (green, light and dark reds), we keep observing a We $\propto$ Bo$^{-0.6}$ scaling for Bo > 0.1, and the singular velocity is reached at lower Bond number, corresponding to lower Laplace number. It is crucial to underline that the Bond number for which the maximum Weber number is obtained depends on the viscosity, which confirms the fact that the Laplace number is the master parameter describing the jet dynamics.

We should emphasize that all scaling laws observed are consistent with each other, within the error bars of the fits. We observe Ca $\propto$ La^{-1}, which implies that $V_{\text{tip}} R_0 \propto \nu$, which means that the velocity of the jet is controlled by viscosity, and $V_{\text{tip}} R_0/\nu$ is constant for a given liquid (i.e., a fixed Morton number). Moreover, by definition we have We $=$ Ca$V_{\text{tip}} R_0/\nu$. Thus, the two scalings laws observed in the data at fixed Morton numbers Ca $\propto$ Bo$^{-0.6}$ and We $\propto$ Bo$^{-0.6}$ are consistent with each other. Also, Ca $\propto$ La^{-1} implies that Ca $\propto$ (Bo/Mo)$^{-1/2}$ and We $\propto$ (Bo/Mo)$^{-1/2}$ close to the observed fitted coefficients.

This closes the comparison-validation between numerical and experimental data. In the remainder of the article we will focus on the analysis of the numerical results and clarify the effect of the Laplace and Bond numbers.

C. The influence of the Bond number: A scaling for the jet velocity, Ca=f(La,Bo)

We have shown previously that our direct numerical simulations capture very well the formation of the jet and its velocity. The Laplace number is the main parameter that sets the jet dynamics, the

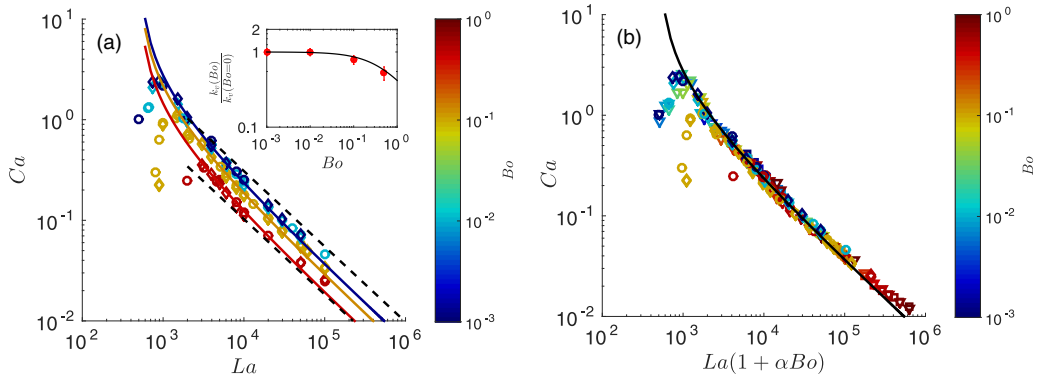

FIG. 6. (a) Jet capillary number Ca as a function of the Laplace number, for four different Bond numbers (Bo = 0.001 in dark blue, Bo = 0.01 in light blue, Bo = 0.1 in yellow, and Bo = 0.5 in red), the Bond number being color-coded. For La > 2000, at a given Laplace number, the velocity increases with decreasing Bond number. The optimal Laplace number for which the highest velocity is observed increases with the Bond number, the highest value of the capillary jet velocity being obtained for small Bond numbers (Bo $\ll$ 0.1). Asymptotically, at high Laplace numbers, the capillary jet velocity scales like Ca $\propto$ La$^{-3/4}$, with a prefactor that depends on the Bond number. Dashed lines are the asymptotic solutions at high Laplace number Ca $\propto$ La$^{-3/4}$. The solid lines are Ca $= k_v(\mathrm{Bo})\mathrm{La}^{-3/4}(\mathrm{La}_*^{-1/2} - \mathrm{La}^{-1/2})^{-3/4}$ [Eq. (5)]. The critical Laplace number is $\mathrm{La}_* = \mathrm{La}_c = 500$, below which no drop ejection is observed. The prefactor $k_v(\mathrm{Bo})$ is fitted to the data and we find $k_v(\mathrm{Bo} = 0) = k_v(\mathrm{Bo} \ll 0.1) = 19$, while at finite Bond number, $k_v(\mathrm{Bo} = 0.1) = 14$ and $k_v(\mathrm{Bo} = 0.5) = 10$. Inset shows $k_v(\mathrm{Bo})$, with the fitted curve in black $k_v(\mathrm{Bo})/k_v(\mathrm{Bo} = 0) = (1 + \alpha\mathrm{Bo})^{-3/4}$, with $\alpha = 2.2$ fitted to the data. (b) Rescaling with a Bond number correction, Ca as a function of La$(1 + \alpha\mathrm{Bo})$. All DNS data are presented, including the (Bo,Mo) sweep. The solid line describes the regime for La larger than the singularity value, with Ca $= k_v(\mathrm{Bo})\mathrm{La}^{-3/4}(\mathrm{La}_*^{-1/2} - \mathrm{La}^{-1/2})^{-3/4}$, and $k_v(\mathrm{Bo}) = k_v(\mathrm{Bo} = 0)\mathrm{La}_*^{3/8}(1 + \alpha\mathrm{Bo})^{-3/4}$. Diamond and triangles are 2^{12} mesh size, while squares and circles are 2^{11} mesh size.

Bond number induces subtle but significant changes. We now focus on the direct parameter sweep (La,Bo), where the Laplace number is changed, keeping the Bond number constant, and compare our results to recent theoretical findings [32].

Figure 6(a) presents the behavior of the jet capillary number as a function of the Laplace number, four series of data at a given Bond number (instead of Morton number as in Fig. 5). The different Bond numbers appear with different colors as indicated by the color-code on the right. As already discussed before, for any Bond number, at sufficiently low Laplace number, no drop formation is observed. At sufficiently high Laplace number, drops are formed and the jet velocity decreases as the Laplace increases. An optimum is reached for a Laplace number that depends on the Bond number.

For low-enough Bond numbers (Bo $\leqslant$ 0.01), the maximum jet velocity is reached around La = 1000, corresponding to an optimal self-similar focusing and a collapse dynamics close to a finite-time singularity, with a very thin and fast jet. The singularity is in practice regularized by viscous and capillary effects, with viscosity playing a crucial role in the control of this focusing. The fastest jets are obtained for an optimal Laplace number, an explanation of this phenomenon is that the damping action of viscosity shelters the self-similar collapse from short wavelength capillary perturbations, allowing it to come closer to the singular limit and therefore produce faster and thinner jet. For these low Bond numbers, the capillary velocity decreases with La, following a Ca $\propto$ La$^{-3/4}$ scaling for Laplace numbers above the optimal value La $\approx$ 1000. This regime is also observed for higher Bond numbers (Bo $\geqslant$ 0.1), but the maximum velocity is reached at a higher Laplace: La = 1500 corresponds to the maximum velocity for Bo = 0.1, and La = 3000 for Bo = 0.5. In these cases, the maximum velocity is lower than for lower Bond numbers. This indicates that both gravity and viscosity play a role in sheltering the inertiocapillary self-similar collapse. The combination La $\approx$ 1000 and Bo $\approx$ 10^{-2}–10^{-3} provides the best configuration for the collapse to approach as much as

possible the finite-time singularity. Note that this scaling is not incompatible with what we described in Fig. 5, since previously we worked at constant Morton number, which mixes the effect of gravity, surface tension, and viscosity. Here we are able to separate the effect of gravity and we find that the asymptotic scaling at a fixed Bond number follows $\mathrm{Ca} \propto \mathrm{La}^{-3/4}$.

These results can be compared to the recent theoretical work from Gañán-Calvo [32] based on the idea of curvature reversal. In the low Bond number limit ($\mathrm{Bo} \ll 1$), the jet velocity capillary number Ca can be described by $\mathrm{Ca} = k_v \phi^{-3/4}$, where $\phi = (\mathrm{Oh}_* - \mathrm{Oh})\mathrm{Oh}^{-2}$ is a scaling function, and Oh_* is the critical Ohnesorge number for which drop formation stops happening due to viscous effects. Gañán-Calvo [32] obtained $\mathrm{Oh}_* \approx 0.043$ from fit to experimental data in the literature. Since $\mathrm{Oh} = \mathrm{La}^{-1/2}$, this leads to a critical Laplace number $\mathrm{La}_* \approx 550$ close to the value we report, which is $\mathrm{La}_c = 500$. We will use our value of critical Laplace number in the following. The scaling for the velocity can be rewritten as $\phi = (\mathrm{La}_*^{-1/2} - \mathrm{La}^{-1/2})\mathrm{La}$, so that the jet velocity capillary number can be written as

$$\mathrm{Ca} = k_v \mathrm{La}^{-3/4}(\mathrm{La}_*^{-1/2} - \mathrm{La}^{-1/2})^{-3/4}. \tag{5}$$

This relationship describes well the observed numerical and experimental results at fixed Bond number, and indeed, at low Bond number ($\mathrm{Bo} \ll 1$), the constant $k_v = 19$ reaches an asymptotic value and does not depend on gravity. In the high Laplace number limit, $\mathrm{La} \gg \mathrm{La}_*$ (or $\mathrm{Oh} \ll \mathrm{Oh}_*$), we obtain the asymptotic regime $\mathrm{Ca} \approx k_v \mathrm{La}^{-3/4}\mathrm{La}_*^{3/8}$, which is indeed observed at high Laplace numbers. For finite Bond numbers, the asymptotic relation is still observed but with a modified pre-factor, i.e., $k_v(\mathrm{Bo})$ is a function of the Bond number. We find that the prefactor can be described by the following empirical function: $k_v(\mathrm{Bo})/k_v(\mathrm{Bo} = 0) = (1 + \alpha \mathrm{Bo})^{-3/4}$, with $\alpha = 2.2$ a fitted parameter, as plotted in inset of Fig. 6(a). Indeed, far from the optimal Laplace number, the effect of the Bond number can be seen as a correction, while gravity is also shifting the optimal Laplace number. Figure 6(b) shows Ca as a function of $\mathrm{La}(1 + \alpha \mathrm{Bo})$, showing a reasonable rescaling of all data. Therefore, the capillary velocity for all data can be described by the following scaling:

$$\mathrm{Ca} = k_v(\mathrm{Bo})\mathrm{La}^{-3/4}(\mathrm{La}_*^{-1/2} - \mathrm{La}^{-1/2})^{-3/4}, \text{ with } k_v(\mathrm{Bo}) \quad = k_v(\mathrm{Bo} = 0)\mathrm{La}_*^{3/8}(1 + \alpha \mathrm{Bo})^{-3/4}, \tag{6}$$

valid until the optimal Laplace number is reached. Below this optimal Laplace number, which increases with the Bond number, viscosity effects become stronger and the jet velocity decreases as the Laplace is further reduced. Note that, as discussed by Ref. [32], this is compatible with the simulations at $\mathrm{Bo} = 0$ from Duchemin *et al.* [17].

IV. CONCLUSIONS

We have presented high-fidelity direct numerical simulations of the jet dynamics arising from the collapse of a cavity left by a bursting bubble, solving for the axisymmetric two-phase Navier-Stokes equations, for a wide range of Laplace and Bond numbers. The numerical results for the entire duration of the phenomenon are fully converged in terms of grid size, and we show that using an adaptive grid, a resolution equivalent to 2^{13} is necessary to correctly resolve the jet dynamics close to the capillary singularity, while a resolution of 2^{12} is sufficient at higher Laplace numbers. We carefully validate our numerical simulations against recent experimental data [7] for the full dynamical process, from the cavity collapse to the jet formation and the first drop generation. We show that the transient nature of the jet formation process makes the definition of the jet velocity nontrivial, with various definitions in the literature leading to large variations in the reported velocities. We define the jet velocity, as the stationary velocity observed before drop ejection, which is consistent with most of the experimental measurements [7,47]. We discuss the existence and variation of the nondimensionalized jet velocity (Ca and We) for which drop ejection is observed, as a function of nondimensionalized viscosity (La) and gravity (Bo). We find excellent agreement with recent numerical and experimental studies [7,31], for the whole existing range of parameters. We extend this range, especially we explore low Bond numbers ($\mathrm{Bo} < 10^{-2}$), which is hard to reach experimentally. This allows us to discuss scaling laws $\mathrm{We} \propto \mathrm{Bo}^{\beta}$ and $\mathrm{Ca} \propto \mathrm{Bo}^{\beta}$, where β depends on the Bond and Laplace numbers. In the Appendix, we

discuss the importance of the cavity shape on the capillary wave selection process, which strongly modulates the jet tip velocity. We show that this is the main reason why gravity effects need to be taken into account in this problem, since gravity shapes the initial cavity and participates in the capillary wavelength selection process, the velocity of the capillaries having a direct influence on the jet velocity.

Finally, we separate the role of gravity (through the Bond number) and viscosity (through the Laplace number) using our direct numerical simulations. We present a universal formula for the dependence of the jet velocity capillary number as a function of the Laplace and Bond numbers for the entire range explored in this study. We find that the optimal Laplace number depends on the Bond number, and that the highest velocity is reached for vanishing Bond numbers, with viscous effects participating in damping small capillaries, leading to a perfect focusing in space and time of the collapsing cavity energy, well described by a self-similar dynamics, and coming close to the finite-time singularity. This is compatible with earlier discussions [7,17]. Our results at low Bond numbers are in excellent agreement with recent theoretical work [32], based on the idea of curvature reversal and neglecting gravity. We extend this theoretical framework to finite Bond numbers and gravity is seen to have two effects: first it shifts the optimal Laplace number (the optimal Laplace increases with the Bond number), therefore the highest velocity can only be obtained for vanishing Bond numbers (no gravity effects). Second, the capillary jet velocity is decreased when gravity becomes important (due to the change in the initial cavity profile and the focusing of the capillaries). This can be empirically incorporated in the theory by allowing for the prefactor to vary with the Bond number, and all data above the optimal Laplace number can be described by $\mathrm{Ca} = k_v(\mathrm{Bo})\mathrm{La}^{-3/4}(\mathrm{La}_*^{-1/2} - \mathrm{La}^{-1/2})^{-3/4}$, with $k_v(\mathrm{Bo}) = k_v(\mathrm{Bo}=0)\mathrm{La}_*^{3/8}(1+\alpha\mathrm{Bo})^{-3/4}$. While the work from Ref. [32] has provided a framework to describe the jet velocity without gravity effects, a theoretical explanation for the correction due to gravity and the change in the focusing path of the capillaries, as well as the change of the optimal viscosity for jetting remain open questions.

This work provides universal formula for the jet velocity of bursting bubbles for all Laplace and Bond numbers, which controls the velocity of the ejected drops. This provides a first step in computing the part of air-sea fluxes due to bursting. We are in the process of extending this work for the size and velocity of the ejected droplets and hope to report about those results in subsequent publications.

ACKNOWLEDGMENTS

L.D. acknowledges support from the Princeton Environmental Institute at Princeton University and the Urban Grand Challenge program. Computations were partially performed using allocation TG-OCE140023 to L.D. from the Extreme Science and Engineering Discovery Environment (XSEDE), which is supported by NSF Grant No. ACI-1053575. We were made aware of the work of Alfonso Gañán-Calvo during the final revisions of the paper and acknowledge discussions during the 2017 APS-DFD meeting in Denver. We thank Jens Eggers for discussions.

APPENDIX: IMPORTANCE OF THE INITIAL CAVITY SHAPE ON THE JET DYNAMICS

In this Appendix, we discuss the importance of the initial shape of the cavity on the jet velocity. We show that we need to consider the real static bubble shape, and not a simplified spherical cavity, to obtain realistic jet velocity. Indeed, even a small modification of the cavity shape will change the selected wavelengths of the capillaries that propagates toward the apex of the cavity, and, consequently, the jet shape and velocity. We test the influence of the initial shape of the cavity for two Bond numbers in air-water conditions: a small Bond number ($\mathrm{Bo} = 0.01$) and a relatively large Bond number ($\mathrm{Bo} = 0.1172$). Four cavity shapes are used:

(i) the static bubble shape computed theoretically by solving the Young-Laplace equations, which corresponds to the observed bubble (shown in blue on Figs. 7 and 8).

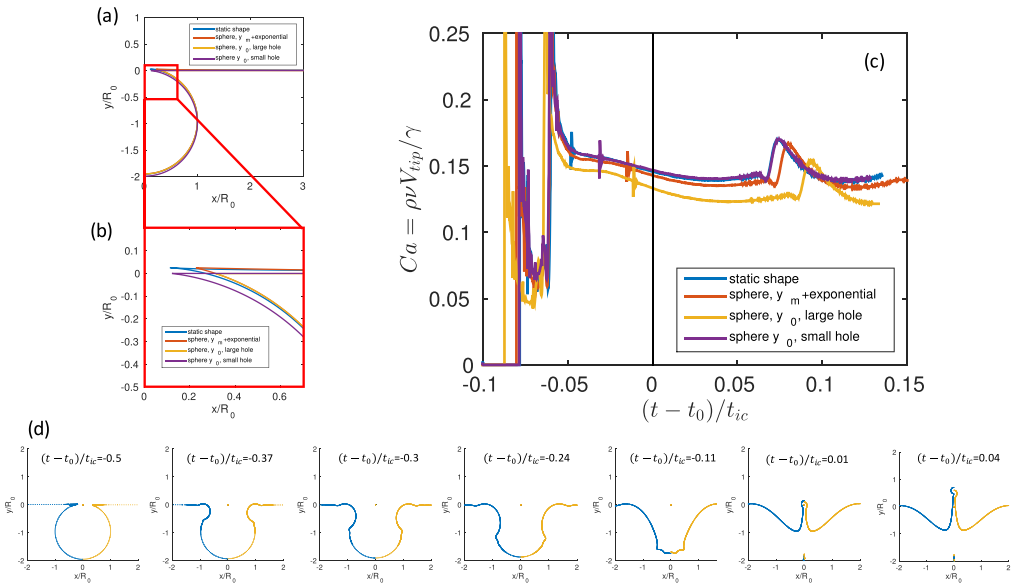

FIG. 7. Influence of the initial cavity shape on the jet velocity. Bo $= 0.01$ in air-water (Mo $= 2.63 \times 10^{-11}$, La $= 1.96 \times 10^{4}$). (a) Initial shapes of the tested cavity: (i) the static bubble shape, (ii) the spherical cavity with exponential reconnection to the mean level, (iii) the spherical cavity cut at the mean water level, with large hole, (iv) the spherical cavity cut at the mean water level, with small hole. (b) Same figure with a zoom on the cap and hole to see the differences in hole size. (c) Jet capillary number as a function of the normalized time $(t - t_0)/t_{\rm ic}$, for the four cavity shapes. Differences in the final tip velocity as large as 20% can be observed due to the change in the initial conditions. (d) Profiles of two cavities (static bubble shape and large hole) at different times, showing that the generated capillaries have different wavelengths when the hole size changes. Shorter capillary waves are selected for a smaller hole (static case), leading to faster waves, leading to a faster jet.

(ii) a spherical cavity with exponential reconnection to the mean level. The sphere lowest point is placed at the same depth as in the static solution and it is connected to an exponential meniscus at the free surface, shown as orange profiles on Figs. 7 and 8. This means the size of the hole at the top is slightly larger but the shape is otherwise similar.

(iii) a spherical cavity cut at the mean water level, with large hole. The sphere lowest point is placed at the same depth as the static solution, the sphere is then cut when it reaches the mean water level. The connection to the mean water level is flat. This gives a larger hole than in the static case. This profile is shown in yellow on Figs. 7 and 8.

(iv) a spherical cavity cut at the mean water level, with the correct hole. The sphere lower part is placed so that the size of the hole matches the static hole. The connection to the mean water level is flat. This gives a hole the same size as the static case. This profile is shown in purple on Figs. 7 and 8.

All these choices are arbitrary but lead to variations in the size of the hole and the way the hole is connected to the mean water level, which are the main geometrical properties of the cavity which influence the initial generation, and then the propagation and focusing of capillary waves inside the cavity.

Figures 7 and 8 show the profile of the initial cavity for the four cases defined above (a, b), as well as the jet capillary number as a function of time (c), and the comparisons of time evolutions of the cavity profiles (i) and (iii) (d). We run these four cavity shape scenarios for two different Bond numbers: Bo $= 0.01$ for Fig. 7 and Bo $= 0.1172$ for Fig. 8.

For a low Bond number (Bo $= 0.01$) the differences between the cavity shapes are subtle, and visible mainly when zooming on the hole size [Fig. 7(b)]. Therefore, the low Bond number case

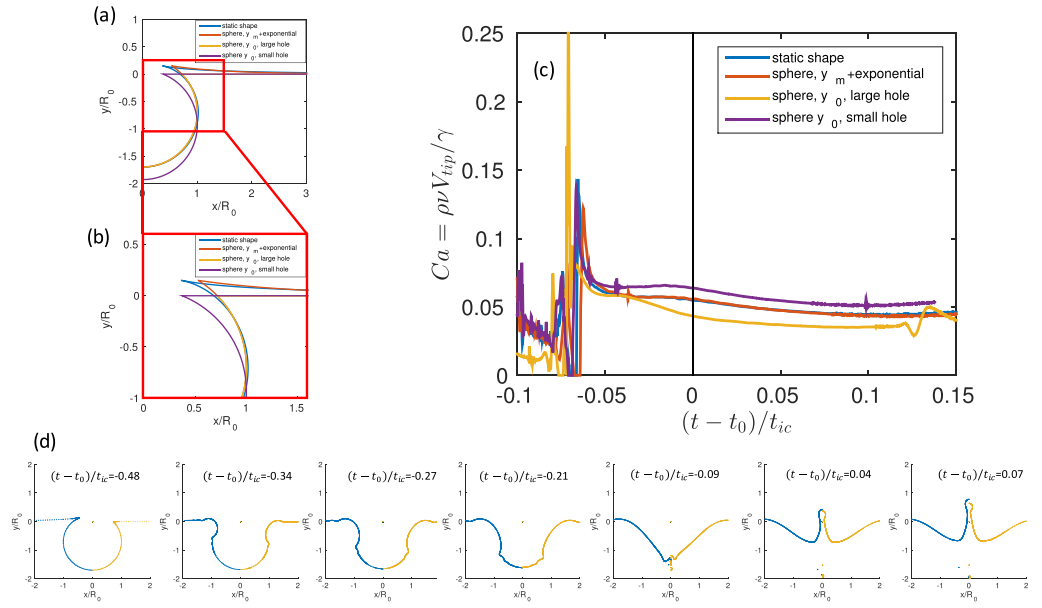

FIG. 8. Influence of the initial cavity shape on the jet velocity. Bo = 0.1172 in air-water (Mo = 2.63×10^{-11}, La = 7×10^4). (a) Initial shapes of the tested cavity: (i) the static bubble shape, (ii) the spherical cavity with exponential reconnection to the mean level, (iii) the spherical cavity cut at the mean water level, with large hole, (iv) the spherical cavity cut at the mean water level, with small hole. (b) Same figure with a zoom on the cap and hole to see the differences in hole size. (c) Jet capillary number Ca as a function of the normalized time, $(t - t_0)/t_{ic}$, for the four cavity shapes. Differences in the final tip velocity as large as 30% can be observed due to the change in the initial conditions. (d) Profiles of two cavities (static bubble shape, and large hole) at different times, showing that the generated capillaries have different wavelength when the hole size is changed. Smaller capillaries wavelengths are selected for a smaller hole (static case), leading to faster waves, leading to a faster ejected jet.

primarily tests the influence of the size of the hole on the generated jet. The case with the hole of the same size as the static shape (iv) has a jet velocity very close to the one obtained for the static shape while the other two cases (ii) and (iii) exhibit stronger differences, of the order of 20% for (iii) [Fig. 7(c)]. This shows that at small Bond number, the relatively small size of the initial hole in the cavity is crucial and is a very sensitive parameter in setting the final jet velocity. These differences can be qualitatively explained by the selected capillary waves when the cavity starts to collapse. When looking at the time evolution of the cavity profiles (i) and (iii), we can see that a smaller hole leads to the generation of shorter capillary waves (larger wave numbers), which, given the dispersion relation $c = \omega/k = \sqrt{(\gamma/\rho)k}$, travel faster. These faster waves give birth to a faster jet [Fig. 7(d)].

For the intermediate Bond number (Bo = 0.1172), the differences in the cavity shape are stronger, since the static shape is greatly influenced by gravity and our arbitrary shapes are not. The size of the hole is larger than for the small Bond number case, and the reconnection to the mean water level is very different in the flat and exponential cases [Figs. 8(a) and 8(b)]. The case (ii) is relatively similar to the static shape, while the other two cases (iii) and (iv) are significantly different with changes in the final velocity as large as 30% [Fig. 8(c)]. The hole is relatively large in all cases, which makes changes in this parameter less important, while the reconnection to the mean water level becomes critical. Again, this is related to the generation of capillary waves, which are shorter leading to a faster jet, as shown in the time dependent profiles [Fig. 8(d)].

This section has introduced the role of the capillary wave velocity on the jet tip velocity, with shorter capillary waves traveling faster and leading to faster jets. To conclude, the sensitivity of the

jet velocity on the initial cavity shape is strong and differs for small and intermediate Bond numbers. For small Bond numbers (Bo < 0.1), the cavity is almost spherical and the most important parameter is the size of the hole. For larger Bond numbers (Bo > 0.1), due to gravity, the hole is larger and the static shape maximum is above the mean water level, and it is critical to capture the upper part of the cavity shape (i.e., the way we connect the spherical shape to the mean water level). In all cases, the details of the initial cavity participate in selecting the capillary waves that travel towards the center of the cavity and give rise to the jet. *Shorter capillary waves travel faster and give birth to faster jets*. Therefore, while a simplified cavity shape might give results similar to those observed experimentally in some ranges of Bond and Laplace numbers, it will fail in other ranges. This clearly shows that we have to work with the real static bubble shape when trying to compare to experimental results and determine the velocity of emerging jets in natural conditions.

[1] J. Wu, Production of spume drops by the wind tearing of wave crests: The search for quantification, J. Geophys. Res. **98**, 18221 (1993).

[2] F. Veron, C. Hopkins, E. L. Harrison, and J. A. Mueller, Sea spray spume droplet production in high wind speeds, Geophys. Res. Lett. **39**, L16602 (2012).

[3] D. C. Blanchard, The electrification of the atmosphere by particles from bubbles in the sea, Progr. Oceanogr. **1**, 73 (1963).

[4] D. E. Spiel, More on the births of jet drops from bubbles bursting on seawater surfaces, J. Geophys. Res. **102**, 5815 (1997).

[5] D. E. Spiel, On the births of film drops from bubbles bursting on seawater surfaces, J. Geophys. Res. **103**, 24907 (1998).

[6] J. Wu, Production functions of film drops by bursting bubbles, J. Phys. Oceanogr. **31**, 3249 (2001).

[7] E. Ghabache, A. Antkowiak, C. Josserand, and T. Séon, On the physics of fizziness: How bubble bursting controls droplets ejection, Phys. Fluids **26**, 121701 (2014).

[8] G. B. Deane and M. D. Stokes, Scale dependence of bubble creation mechanisms in breaking waves, Nature **418**, 839 (2002).

[9] L. Deike, W. K. Melville, and S. Popinet, Air entrainment and bubble statistics in breaking waves, J. Fluid Mech. **801**, 91 (2016).

[10] L. Deike, L. Lenain, and W. K. Melville, Air entrainment by breaking waves, Geophys. Res. Lett. **44**, 3779 (2017).

[11] E. L. Andreas, J. B. Edson, E. C. Monahan, M. P. Rouault, and S. D. Smith, The spray contribution to net evaporation from the sea: A review of recent progress, Boundary-Layer Meteorol. **72**, 3 (1995).

[12] E. R. Lewis and S. E. Schwartz, *Sea Salt Aerosol Production. Mechanisms, Methods, Measurements, and Models*, geophysical monograph 152 (American Geophysical Union, Washington, DC, 2004).

[13] G. de Leeuw, E. L. Andreas, M. D. Anguelova, C. W. Fairall, E. R. Lewis, C. O'Dowd, M. Schulz, and S. E. Schwartz, Production flux of sea spray aerosol, Rev. Geophys. **49**, RG2001 (2011).

[14] F. Veron, Ocean spray, Annu. Rev. Fluid Mech. **47**, 507 (2015).

[15] H. Lhuissier and E. Villermaux, Bursting bubble aerosols, J. Fluid Mech. **696**, 5 (2012).

[16] F. MacIntyre, Flow patterns in breaking bubbles, J. Geophys. Res. **77**, 5211 (1972).

[17] L. Duchemin, S. Popinet, C. Josserand, and S. Zaleski, Jet formation in bubbles bursting at a free surface, Phys. Fluids **14**, 3000 (2002).

[18] E. Ghabache and T. Séon, Size of the top jet drop produced by bubble bursting, Phys. Rev. Fluids **1**, 051901(R) (2016).

[19] X. Wang, G. B. Deane, K. A. Moore, O. S. Ryder, M. D. Stokes, C. M. Beall, D. B. Collins, M. V. Santander, S. M. Burrows, C. M. Sultana, and K. A. Prather, The role of jet and film drops in controlling the mixing state of submicron sea spray aerosol particles, Proc. Natl. Acad. Sci. **114**, 6978 (2017).

[20] R. H. Pierce, M. S. Henry, P. C. Blum, S. L. Hamel, B. Kirkpatrick, Y. S. Cheng, Y. Zhou, C. M. Irvin, J. Naar, A. Weidner, L. E. Fleming, L. C. Backer, and D. G. Baden, Brevetoxin composition in water and

marine aerosol along a florida beach: Assessing potential human exposure to marine biotoxins, Harmful Algae **4**, 965 (2005).
[21] P. L. L. Walls, J. C. Bird, and L. Bourouiba, Moving with bubbles: A review of the interactions between bubbles and the microorganisms that surround them, Integr. Comp. Biol. **54**, 1014 (2014).
[22] G. Liger-Belair, C. Cilindre, R. D. Gougeon, M. Lucio, I. Gebefügi, P. Jeandet, and P. Schmitt-Kopplin, Unraveling different chemical fingerprints between a champagne wine and its aerosols, Proc. Natl. Acad. Sci. USA **106**, 16545 (2009).
[23] T. Séon and G. Liger-Belair, Effervescence in champagne and sparkling wines: From bubble bursting to droplet evaporation, Eur. Phys. J. Special Topics **226**, 117 (2017).
[24] A. H. Woodcock, C. F. Kientzler, A. B. Arons, and D. C. Blanchard, Giant condensation nuclei from bursting bubbles, Nature **172**, 1144 (1953).
[25] M. P. Brenner, Fluid mechanics: Jets from a singular surface, Nature **403**, 377 (2000).
[26] B. W. Zeff, B. Kleber, J. Fineberg, and D. P. Lathrop, Singularity dynamics in curvature collapse and jet eruption on a fluid surface, Nature **403**, 401 (2000).
[27] J. M. Boulton-Stone and J. R. Blake, Gas bubbles bursting at a free surface, J. Fluid Mech. **254**, 437 (1993).
[28] H. N. Oguz and A. Prosperetti, Dynamics of bubble growth and detachment from a needle, J. Fluid Mech. **257**, 111 (1993).
[29] A. Prosperetti and H. N. Oguz, The impact of drops on liquid surfaces and the underwater noise of rain, Annu. Rev. Fluid Mech. **25**, 577 (1993).
[30] M. S. Longuet-Higgins and H. Oguz, Critical microjets in collapsing cavities, J. Fluid Mech. **290**, 183 (1995).
[31] P. L. L. Walls, L. Henaux, and J. C. Bird, Jet drops from bursting bubbles: How gravity and viscosity couple to inhibit droplet production, Phys. Rev. E **92**, 021002(R) (2015).
[32] A. M. Gañán-Calvo, Revision of Bubble Bursting: Universal Scaling Laws of Top Jet Drop Size and Speed, Phys. Rev. Lett. **119**, 204502 (2017).
[33] E. Ghabache, G. Liger-Belair, A. Antkowiak, and T. Séon, Evaporation of droplets in a champagne wine aerosol, Sci. Rep. **6**, 25148 (2016).
[34] E. Ghabache, Surface libre hors équilibre : de l'effondrement de cavité aux jets étirés, Ph.D. thesis, UPMC (2015).
[35] S. Popinet, Gerris: A tree-based adaptive solver for the incompressible euler equations in complex geometries, J. Comput. Phys. **190**, 572 (2003).
[36] S. Popinet, An accurate adaptive solver for surface-tension-driven interfacial flows, J. Comp. Phys. **228**, 5838 (2009).
[37] D. Fuster, G. Agbaglah, C. Josserand, S. Popinet, and S. Zaleski, Numerical simulation of droplets, bubbles and waves: State of the art, Fluid Dynam. Res. **41**, 065001 (2009).
[38] X.-D. Chen, D.-J. Ma, V. Yang, and S. Popinet, High-fidelity simulations of impinging jet atomization, Atomiz. Sprays **23**, 1079 (2013).
[39] D. Fuster, J. P. Matas, S. Marty, S. Popinet, J. Hoepffner, A. Cartellier, and S. Zaleski, Instability regimes in the primary breakup region of planar coflowing sheets, J. Fluid Mech. **736**, 150 (2013).
[40] L. Deike, S. Popinet, and W. K. Melville, Capillary effects on wave breaking, J. Fluid Mech. **769**, 541 (2015).
[41] L. Deike, N. Pizzo, and W. K. Melville, Lagrangian transport by breaking surface waves, J. Fluid Mech. **829**, 364 (2017).
[42] L. Deike, D. Fuster, M. Berhanu, and E. Falcon, Direct Numerical Simulations of Capillary Wave Turbulence, Phys. Rev. Lett. **112**, 234501 (2014).
[43] M.-J. Thoraval, K. Takehara, T. G. Etoh, S. Popinet, P. Ray, C. Josserand, S. Zaleski, and S. T. Thoroddsen, Von Kármán Vortex Street Within an Impacting Drop, Phys. Rev. Lett. **108**, 264506 (2012).
[44] G. Agbaglah and R. D. Deegan, Growth and instability of the liquid rim in the crown splash regime, J. Fluid Mech. **752**, 485 (2014).

[45] J. Hoepffner and G. Paré, Recoil of a liquid filament: Escape from pinch-off through creation of a vortex ring, J. Fluid Mech. **734**, 183 (2013).
[46] S. Krishnan, E. J. Hopfinger, and B. A. Puthenveettil, On the scaling of jetting from bubble collapse at a liquid surface, J. Fluid Mech. **822**, 791 (2017).
[47] D. E. Spiel, On the births of jet drops from bubbles bursting on water surfaces, J. Geophys. Res. **100**, 4995 (1995).